PCCP

Physical Chemistry Chemical Physics

rsc.li/pccp

ChemBos

LModeA

La Ce Pr Nd Pm Sm Eu Gd Tb Dy Ho Er Tm Yb Lu

ROYAL SOCIETY
OF CHEMISTRY
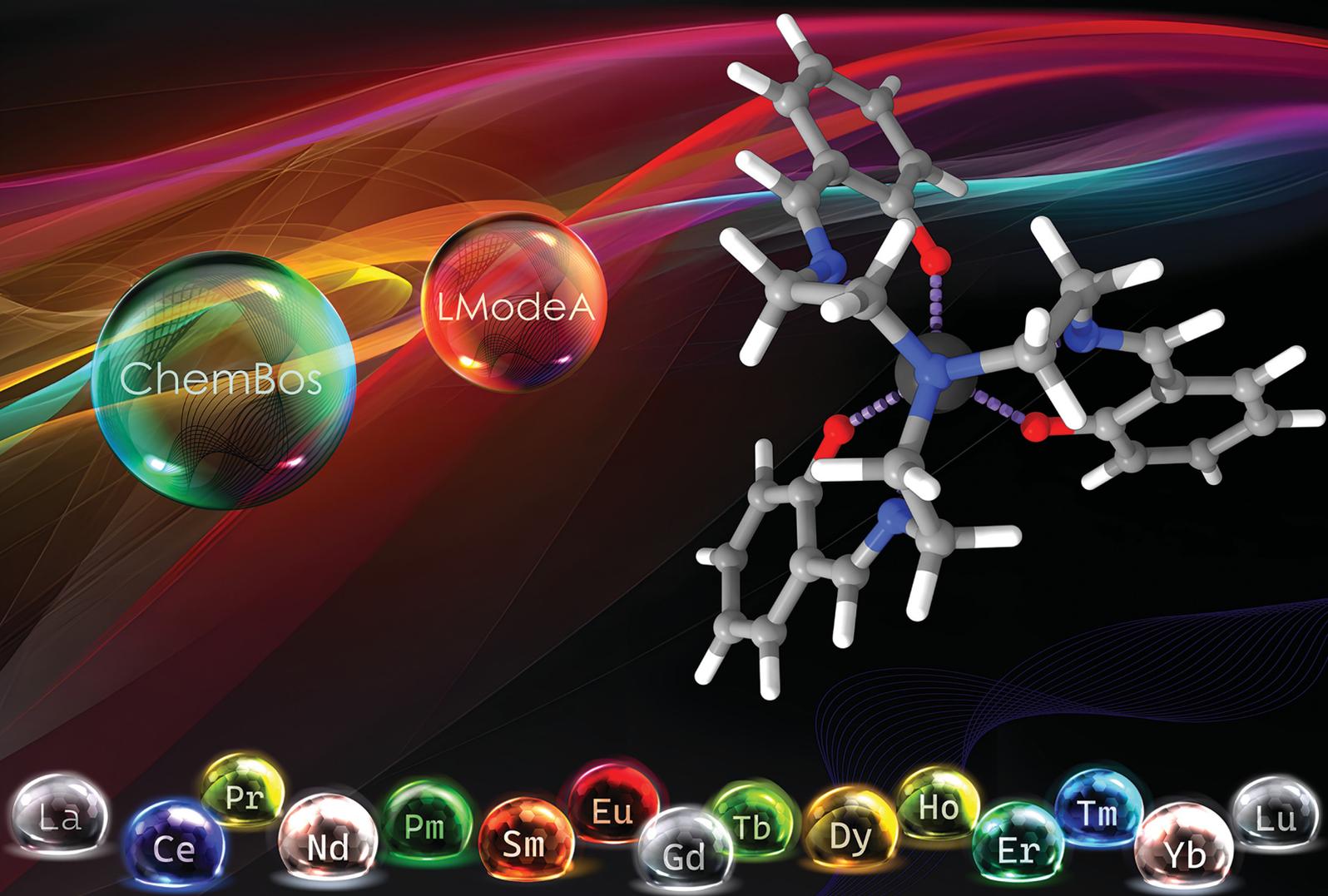
PAPER
Mateus Quintano, Ricardo L. Longo, Renaldo T. Moura Jr. *et al.*
Theoretical insights into the vibrational spectra and chemical
bonding of Ln(III) complexes with a tripodal N_4O_3 ligand
along the lanthanide series

PCCP
Owner Societies

Check for updates

Theoretical insights into the vibrational spectra and chemical bonding of Ln(III) complexes with a tripodal N_4O_3 ligand along the lanthanide series†

Francielle C. Machado, [a] Mateus Quintano, [*ab] Carlos V. Santos-Jr, [c] Albano N. Carneiro Neto, [d] Elfi Kraka, [b] Ricardo L. Longo [*a] and Renaldo T. Moura Jr. [*be]

This study provides new theoretical insights into the vibrational spectra of Ln(III) complexes, along the lanthanide series by utilizing the LModeAGen protocol and integrating cutting-edge topological ideas. It provides a quantitative interpretation of the vibrational spectra of [Ln(trensal)] complexes at the B3LYP/MWBn(Ln)/6-311++G** (n from 46 (La) to 60 (Lu)) level using the characterization of normal modes from the local vibrational mode theory. This involves decomposing normal vibrational modes related to the complex formation, distortions in the coordination sphere, and C−H vibrations into local mode contributions, offering particularly promising results aimed at the design of highly luminescent lanthanide complexes. This study also delivers key theoretical insights into the chemical bonding of the coordination sphere of [Ln(trensal)] by combining the local vibrational mode theory and the bond overlap model to achieve relationships between bond properties, including those of the Badger-type. Altogether, we present the theoretical framework necessary to quantitatively interpret the vibrational spectra of [Ln(trensal)] complexes along the lanthanide series and gain a better understanding of the lanthanide-ligand chemical bonds, thereby enhancing our understanding of their chemistry and guiding future design efforts.

Introduction

Rare earth elements, 15 of which belong to the lanthanide (La–Lu) series, are present in moderate amounts in the lithosphere and have special attributes that make them useful in catalysts, lasers, magnets, batteries, and even biological applications.[1–5] From a chemistry perspective, a better understanding of chemical bonding in lanthanide-containing compounds should facilitate these applications.[6] To this end, we have employed the local vibrational mode (LVM) theory, originally proposed by Konkoli and Cremer,[7] and the bond overlap model (BOM)[8–10] for investigating Ln(III)

a Departamento de Química Fundamental, Universidade Federal de Pernambuco, Cidade Universitária, 50740-560, Recife, PE, Brazil. E-mail: mateusmquintano@gmail.com, ricardo.longo@ufpe.br

b Computational and Theoretical Chemistry Group (CATCO), Department of Chemistry, Southern Methodist University, Dallas, TX 75275, USA. E-mail: renaldotmjr@gmail.com

c Department of Chemistry, Federal University of Paraíba, João Pessoa, PB 58033-455, Brazil

d Physics Department and CICECO – Aveiro Institute of Materials University of Aveiro, Aveiro 3810-193, Portugal

e Department of Chemistry and Physics, Center of Agrarian Sciences, Federal University of Paraíba, Areia, PB 58397-000, Brazil

† Electronic supplementary information (ESI) available. See DOI: https://doi.org/10.1039/d4cp03677h

ions in complexes with the tripodal trensal ligand[11] (see Fig. 1a) along the La–Lu series. This investigation of the entire series is expected to contribute to the fundamental chemistry of Pm(III), which is quite unknown.[12]

Trivalent lanthanide ions, Ln(III), possess a unique electronic structure, which distinguishes them from other elements as their 4f valence orbitals are shielded by the filled 5s and 5p orbitals, isolating the 4f electrons from external chemical influences.[5,13] The trensal ligand coordinates Ln(III) in the trianionic heptadentate (N_4O_3) form.[14–18] Due to the C_3 point symmetry, the coordination sphere of the resulting complex, [Ln(trensal)] (see Fig. 1b), can be divided into three distinct families: the Ln–O, Ln–N, and Ln–N′ fragments.[15] N′ denotes the apical nitrogen atom (within the C_3 axis), which is non-equivalent to the other three nitrogen atoms and is expected to be unbound in complexes of first-row transition metals due to a decrease in denticity to six.[16,18]

The formation of [Ln(trensal)] is experimentally confirmed by a strong infrared (IR) band attributed to C=N stretch.[14,15,19–23] Consequently, the sensitivity of IR spectroscopy to lanthanide coordination can be linked to specific normal vibrational modes within the fingerprint region of the vibrational spectra. However, the high delocalization of normal vibrational modes makes it difficult to pinpoint specific bond stretching contributions, as
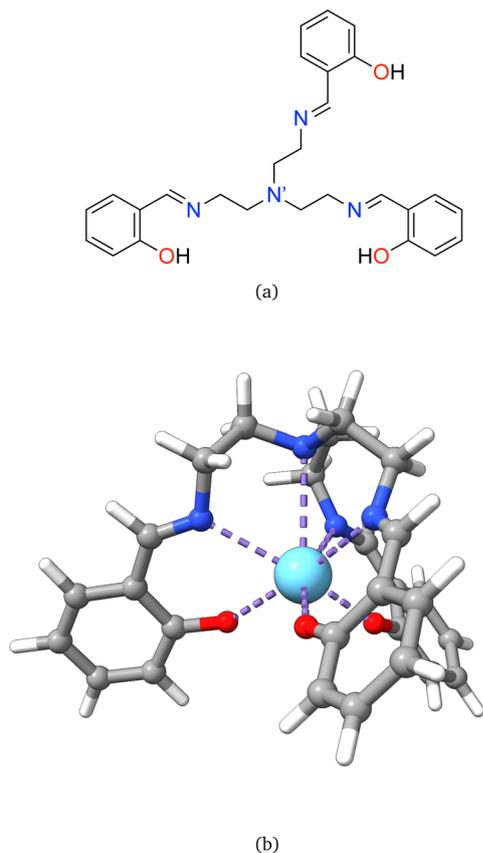
Fig. 1 (a) Schematic 2D representation of the neutral form of the unbound trensal ligand (H_3 trensal), and (b) the 3D visualization of trensal bound to a trivalent lanthanide ion (oxygen, nitrogen, lanthanide, carbon, and hydrogen are depicted in red, blue, light blue, grey, and white, respectively).

extensively emphasized in the literature by some of us in the context of various chemical systems.[8,24–30] In other words, assigning the strong IR characteristic band typical of [Ln(trensal)] solely to the imine C=N stretching vibration, without quantitative spectral analysis, is incomplete due to the delocalization conundrum.

Delocalization also hinders the study of Badger-type relationships,[31,32] as the correlation with bond lengths requires breaking down polyatomic molecules into quasi-diatomic molecules[31] (or recently referred to as "diatomics within molecules"[33]) to obtain local mode properties such as frequencies or force constants. In this respect, relationships between bond properties can enhance our understanding of chemical bonding, especially when different quantum chemistry methods can be employed for analysis. Our combined protocol, which integrates LVM with BOM, exemplifies this approach. Often, one bond property is easily obtained experimentally, while another is more challenging to assess. For example, measuring or calculating the vibrational spectrum of a compound is typically more practical than performing a detailed structural analysis.[31] In cases like that of Pm, where experimental data on chemical bonding is unavailable,[12] vibrational spectroscopy is expected to become an invaluable tool for gaining insights into bond properties.

Furthermore, recent interest in designing luminescent lanthanide complexes has focused on identifying the normal vibrational modes, calculated at the density functional theory[34] (DFT) level in the gas phase, most strongly coupled to the electronic states, which for [Yb(trensal)] are mainly within the frequency range of 0–500 cm^{-1} and simultaneously distort the first coordination sphere while breaking the C_3 symmetry of the molecule.[35] Moreover, the design should take into consideration the character of the vibrational modes that lead to non-radiative deactivation of excited states.[13] To take a case in point, the C–H vibrations exhibiting significant anharmonicity in [Eu(trensal)], for instance, can give rise to the undesired dissipation pathway of the excitation energy.[36] As a result, the normal mode decomposition of the C–H related region of the IR spectrum is germane to our approach as well.

So far, a theoretical framework that aids in the elucidation of the vibrational spectra of [Ln(trensal)] complexes along the lanthanide series has been lacking and is of paramount interest for gaining a better understanding of the lanthanide chemistry involved. This clearly calls for new ideas to facilitate the quantitative spectral analysis *via* normal mode decomposition. In this work, we have addressed this need by utilizing the characterization of normal mode (CNM) procedure,[25,37,38] an integral part of the LVM theory, as a key tool.

It is worth mentioning as a motivation that the recent application of local mode analysis in lanthanide spectroscopy has provided new insights into the degree of normal mode delocalization and the bonding behavior within the coordination sphere of lanthanide complexes.[8] To the best of our knowledge, the present study presents for the first time a complete characterization of the [Ln(trensal)] complexes along the La–Lu series by the combined computational approach herein proposed, aiming to give:

(i) A quantitative interpretation *via* CNM spanning the gas-phase DFT-computed IR spectra to elucidate the normal vibrational modes associated with peaks linked to distortion within the first coordination sphere with disruption of the C_3 symmetry, complex formation, and C–H vibrations.

(ii) A comparative analysis involving the local mode force constant, the ligand effective polarizability from BOM, bond distances, and ionic radii to gain a better understanding of chemical bonding within the coordination sphere.

(iii) A pairwise comparison between [Er(trensal)] and [Fe(trensal)] to probe the change in bonding of the trensal ligand by the apical nitrogen using the local mode force constant.

Methodology

Normal mode analysis

According to the GF method,[39,40] the Lagrangian $\mathcal{L}$ for a polyatomic molecule composed of N atoms undergoing harmonic vibrations can be conveniently expressed using the following matrix formulation:

$$\mathcal{L} = \frac{1}{2}\dot{\mathbf{q}}^{\dagger}\mathbf{G}^{-1}\dot{\mathbf{q}} - \frac{1}{2}\mathbf{q}^{\dagger}\mathbf{F}^{q}\mathbf{q} \qquad (1)$$

This journal is © the Owner Societies 2025

Phys. Chem. Chem. Phys., 2025, **27**, 1794–1803 | **1795**

PCCP

Paper

The quadratic form of both kinetic and potential energies satisfies the Euler-Lagrange equation, ensuring the existence of an extremum for each internal coordinate q_n ($n = 1,\ldots, N_{\mathrm{vib}}$):

$$\frac{\mathrm{d}}{\mathrm{d}t}\frac{\partial \mathcal{L}}{\partial \dot{q}_n} - \frac{\partial \mathcal{L}}{\partial q_n} = 0 \qquad (2)$$

The matrices G and F^q, both of size $N_{\mathrm{vib}} \times N_{\mathrm{vib}}$, represent the Wilson G matrix and the Hessian matrix in internal coordinates q, respectively. These matrices are simultaneously diagonalizable by $\tilde{\mathbf{D}}$. The internal coordinate vector $\mathbf{q}$ can be defined as the result of a linear transformation $\tilde{\mathbf{D}}$ applied to the normal coordinate vector $\mathbf{Q}$, expressed as:

$$\mathbf{q} = \tilde{\mathbf{D}}\mathbf{Q} \qquad (3)$$

The normal vectors $\tilde{\mathbf{d}}_\mu$ ($\mu = 1,\ldots,N_{\mathrm{vib}}$) in internal coordinates constitute the columns of the matrix $\tilde{\mathbf{D}}$.

The vibrational secular equation in internal coordinates is expressed as:

$$\mathbf{F}^q\tilde{\mathbf{D}} = \mathrm{G}^{-1}\tilde{\mathbf{D}}\boldsymbol{\Lambda} \qquad (4)$$

The subsequent equality, involving the identity matrix $\mathbf{I}$, holds:

$$\tilde{\mathbf{D}}^\dagger \mathrm{G}^{-1}\tilde{\mathbf{D}} = \mathbf{I} \qquad (5)$$

The diagonal matrix $\boldsymbol{\Lambda}$ comprises N_{vib} eigenvalues λ_μ, corresponding to N_{vib} frequency values ω_μ (in cm^{-1}):

$$\omega_\mu = \frac{1}{2\pi c}\lambda_\mu^{1/2} \qquad (6)$$

with c being the speed of light in vacuum. Stated differently, the set of diagonal elements λ_μ of the matrix $\boldsymbol{\Lambda}$ produces the vibrational spectrum of a polyatomic molecule.

The Wilson B matrix, represented as a $N_{\mathrm{vib}} \times 3N$ rectangular matrix, incorporates the first derivatives of the internal coordinates q_n ($n = 1,\ldots,N_{\mathrm{vib}}$) with respect to the Cartesian coordinates x_i ($i = 1,\ldots,3N$) as its elements B_{ni}. This matrix serves to establish the connection between internal and Cartesian coordinates:[39]

$$\mathbf{q} = \mathbf{B}x \qquad (7)$$

$$B_{ni} = \frac{\partial q_n}{\partial x_i} \qquad (8)$$

The pseudo-inverse matrix of $\mathbf{B}$ is the matrix $\mathbf{C}$:[38]

$$\mathbf{C} = \mathbf{M}^{-1}\mathbf{B}^\dagger \mathrm{G}^{-1} \qquad (9)$$

The matrix $\mathbf{M}$ represents the mass matrix, structured as a $3N \times 3N$ matrix, where each atomic mass is repeated three times to account for motion in the x, y, and z directions.

Renormalization of $\tilde{\mathbf{D}}$, via the diagonal matrix $\mathbf{M}^R$ of reduced mass elements m_μ^R, in conformity with

$$\mathbf{D} = \tilde{\mathbf{D}}(\mathbf{M}^R)^{1/2} \qquad (10)$$

results in

$$\mathbf{D}^\dagger \mathrm{G}^{-1}\mathbf{D} = \mathbf{M}^R \qquad (11)$$

$$\mathbf{D}^\dagger \mathbf{F}^q\mathbf{D} = \mathbf{K} \qquad (12)$$

by recasting eqn (5) and (4), respectively. Here, $\mathbf{D}$ represents the column-wise grouping of the normal vectors $\mathbf{d}_\mu$, and $\mathbf{K}$ denotes the diagonal matrix of normal force constants, defined as $\mathbf{K} = \mathbf{F}^Q$. Another connection between internal and Cartesian coordinates is provided by

$$\mathbf{F}^q = \mathbf{C}^\dagger \mathbf{F}^x\mathbf{C} \qquad (13)$$

$$\mathbf{L} = \mathbf{C}\mathbf{D} \qquad (14)$$

Clearly, $\mathbf{L}$ gathers the normal vectors $\mathbf{l}_\mu$ within its columns.

Multiplying eqn (3) from the left by $\tilde{\mathbf{D}}^\dagger \mathrm{G}^{-1}$, taking into account eqn (5), yields:

$$\mathbf{Q} = \tilde{\mathbf{D}}^\dagger \mathrm{G}^{-1}\mathbf{q} \qquad (15)$$

In other words, normal coordinates are linear combinations of internal coordinates. This results in normal vibrational modes typically spread out across the molecule, thereby restricting the utility of normal mode frequencies and force constants as measures of bond strength. To address this, local vibrational modes and their corresponding frequencies and force constants are necessary. The delocalization also renders it impractical to track subtle structural changes and variations in the molecule's surroundings without a method for normal mode decomposition. In this regard, the CNM procedure emerges as a novel and powerful tool as an integral part of the LVM theory. It offers a quantitative approach to decomposing normal vibrational modes into local mode contributions. As a result, it facilitates the quantitative analysis of vibrational spectra, offering insights into the molecular fragments involved in a novel and innovative manner.

Local mode analysis

The local mode vectors $\mathbf{a}_n$ associated with the internal coordinates q_n can be calculated utilizing the normal vibrational modes $\mathbf{d}_n$ and the diagonal force constant matrix $\mathbf{K}$, as demonstrated by Konkoli and Cremer in their seminal paper on the local vibrational mode theory:[7]

$$\mathbf{a}_n = \frac{\mathbf{K}^{-1}\mathbf{d}_n^\dagger}{\mathbf{d}_n\mathbf{K}^{-1}\mathbf{d}_n^\dagger} \qquad (16)$$

Obtaining $\mathbf{d}_n$ and $\mathbf{K}$ is a standard procedure in modern quantum chemistry packages after a vibrational frequency calculation. Transformation to the Cartesian coordinate space can be performed by means of $\mathbf{L}$ to give $\mathbf{a}_n^x$:

$$\mathbf{a}_n^x = \mathbf{L}\mathbf{a}_n \qquad (17)$$

The local mode force constant k_n^{a} can be calculated as:

$$k_n^{\mathrm{a}} = \mathbf{a}_n^\dagger \mathbf{K}\mathbf{a}_n = (\mathbf{d}_n\mathbf{K}^{-1}\mathbf{d}_n^\dagger)^{-1} \qquad (18)$$

It should be noted that Zou and Cremer proposed k_n^{a} as a local descriptor of the intrinsic strength of the bond or non-covalent interaction between two atoms under consideration.[41] Furthermore, the local force constant enables the generalization of Badger's rule, establishing a universal relationship between interatomic distance (R) and the corresponding local force constant, provided that all bonds considered exhibit similar electronic features.[31] The local mode frequency ω_n^{a} can then be

1796 | *Phys. Chem. Chem. Phys.*, 2025, **27**, 1794–1803

This journal is © the Owner Societies 2025

calculated:

$$(\omega_n^{\mathrm{a}})^2 = (4\pi^2 c^2)^{-1}\frac{k_n^{\mathrm{a}}}{m_n^{\mathrm{a}}} \qquad (19)$$

with m_n^{a} being the local mode mass, which can be computed in terms of the diagonal element of $\mathbf{G}$:

$$m_n^{\mathrm{a}} = \frac{1}{G_{nn}} \qquad (20)$$

Each normal vibrational mode, including those of significant interest corresponding to peaks in the vibrational spectrum, can be decomposed into the percentage contributions of non-redundant local vibrational modes from a complete set using the characterization of normal mode procedure.[26,30] This is based on an adiabatic connection scheme (ACS).[42] The degree of overlap, represented by $S_{n\mu}$,[25,37,38] is defined as:

$$S_{n\mu} = \frac{\left\langle \mathbf{a}_n^x | \mathbf{F}^x | \mathbf{l}_\mu \right\rangle^2}{\left\langle \mathbf{a}_n^x | \mathbf{F}^x | \mathbf{a}_n^x \right\rangle \left\langle \mathbf{l}_\mu | \mathbf{F}^x | \mathbf{l}_\mu \right\rangle} \qquad (21)$$

with $\mathbf{a}_n^x$, $\mathbf{F}^x$, and $\mathbf{l}_\mu$ representing the local vibrational mode, the Hessian matrix, and the normal vibrational mode in Cartesian coordinates, respectively. The percentage contribution $C_{n\mu}^{\%}$ (local mode contribution) of the local vibrational mode $\mathbf{a}_n^x$ to the normal vibrational mode $\mathbf{l}_\mu$ is then attained as follows:[37]

$$C_{n\mu}^{\%} = \frac{S_{n\mu}}{\sum\limits_{m}^{N_{\mathrm{vib}}} S_{m\mu}}100 \qquad (22)$$

A CNM plot illustrates normal mode decompositions, with the local mode contributions $C_{n\mu}^{\%}$ shown as distinct components forming the bars that represent the normal modes in a diagram. The normal frequencies corresponding to the decomposed normal modes are displayed on the plot's x-axis. For further details on the LVM theory, the reader is referred to two comprehensive feature articles.[25,38]

The following set of formulas defines the number of bond (N_{b}), angle (N_{a}), and dihedral (N_{d}) parameters necessary to form a topologically complete and non-redundant set of local vibrational modes for CNM[30] and implemented in LModeAGen:[26]

$$N_{\mathrm{b}} = N + f - 2 \qquad (23)$$

$$N_{\mathrm{a}} = N - f - 1 \qquad (24)$$

$$N_{\mathrm{d}} = N - 3 \qquad (25)$$

From the perspective of graph theory, f represents the number of faces of the molecular graph, whether it is of tree, cycle, or polyhedral type.[30]

Given both the significant delocalization observed in the normal vibrational modes associated with the infrared-active peaks and the dimension of the vibrational space of the Ln-containing complexes along the La–Lu series, it is recommended to perform the CNM analysis using local mode families. For the C–H family, this involves merging all the percentage contributions of C–H local modes, $\sum\limits_{n} C_n^{\%}(\mathrm{C} - \mathrm{H})$, to form the C–H entry in Fig. 6. A similar rationale applies to

other local mode families. For visualization purposes, $\varSigma\sigma$ comprises the summation of all σ local mode contributions below the threshold of 5%.

Ligand effective polarizability

The bond overlap model (BOM)[9,10] explains the dynamic coupling (DC) mechanism[43–45] *via* overlap and ligand effective polarizabilities ($\alpha = \alpha' + \alpha_{\mathrm{OP}}$), with α_{OP} and α' denoting bond overlap polarization and ligand polarizability contributions to DC, respectively.[9,10] Improved effective ligand polarizabilities (α') are obtained by decomposing the molecular polarizability for the entire complex into localized molecular orbitals (LMOs) contributions, which are relevant for understanding ligand interactions with Ln(III).[8] It should be mentioned that BOM has recently been implemented for multiconfigurational wave functions.[46] For up-to-date applications of BOM, readers are referred to the recent literature.[47–53]

Computational details

The complexes formed with the trensal ligand[14–17] binding to Ln(III) ions from lanthanum to lutetium were investigated. Very little has been found in the literature on Pm, which highlights the importance of this investigation encompassing the entire series. Equilibrium geometries, Hessian matrices, and associated normal vibrational modes, as well as finite field calculations, employed the B3LYP[54,55] functional in combination with the 6-311++G** basis set[56,57] to describe all ligand atoms as well as a pseudopotential scheme (MWBn, n varies with atomic number)[58] and valence electrons basis set for Ln(III) ions utilizing Gaussian16.[59] For [Fe(trensal)], the results were obtained at the UB3LYP/6-311++G** level. Multiwfn[60] was employed for obtaining the localized molecular orbital (LMO), while ChemBOS[8,47,61] decomposed the molecular polarizability into LMO contributions. The automatic generation of complete and non-redundant sets of local mode parameters was accomplished through the newly developed LModeAGen protocol,[26,30] with local mode analysis being conducted using the standalone LModeA package.[62] All the geometries were visualized using UCSF ChimeraX,[63] and their Cartesian coordinates are provided in the ESI.† The values of trivalent ionic radii used for comparison were taken from the literature.[64] Additionally, in the ESI,† Fig. S3 corroborates the soundness of our model on a comparative basis with the PBE0[65,66] functional.

Results

CNM analysis of selected normal modes

This study aims at assessing the topologically complete and non-redundant set of local vibrational modes[30] for the CNM analysis of the gas-phase DFT-computed vibrational spectra of [Ln(trensal)] complexes at the B3LYP/MWBn(Ln)/6-311++G** level, as implemented in LModeAGen.[26] The molecular graph associated with [Ln(trensal)], featuring $f = 10$, exhibits $N_{\mathrm{b}} = 70$, $N_{\mathrm{a}} = 51$, and $N_{\mathrm{d}} = 59$, with $N_{\mathrm{vib}} = N_{\mathrm{b}} + N_{\mathrm{a}} + N_{\mathrm{d}} = 180$. Fig. 2 shows three out of the ten faces that constitute the associated molecular graph, with the infinite face accounting for the tenth one.[30]
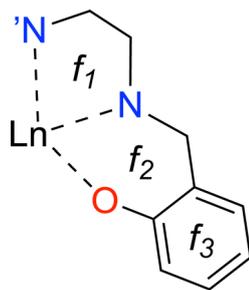
Fig. 2 A 2D representation of one-third of [Ln(trensal)], depicting three out of the ten faces that compose the associated molecular graph.

Fig. 3 shows the gas-phase DFT-computed IR spectrum of [Eu(trensal)], which, albeit slightly blue-shifted, is in considerable agreement with the experimental data extracted from the literature.[36] On average, the IR spectra obtained along the La–Lu series exhibit similar patterns, justifying the selection of a single spectrum for discussion. The peaks identified in the spectrum due to distortion within the first coordination sphere with disruption of the C_3 symmetry (p_1), complex formation (p_2), and C–H vibrations (p_3) are illustrated in Fig. 3.

Distortion within the first coordination sphere (p_1)

As mentioned in the literature, characterizing gas-phase DFT-computed normal vibrational modes strongly coupled to electronic states can be instrumental in designing luminescent lanthanide complexes.[35] For instance, in [Yb(trensal)], these modes fall predominantly within 0–500 cm^{-1}, distorting the first coordination sphere and breaking the C_3 point symmetry.[35] We selected the peak of highest intensity in the frequency range of 0–500 cm^{-1} (p_1) to perform the CNM analysis on the corresponding normal modes along the La–Lu series.

Fig. 4 presents the CNM analysis for the degenerate normal vibrational modes associated with p_1, spanning the frequency range of 196–200 cm^{-1} along the lanthanide series. Consistent with the literature, Fig. 4 agrees with the previous report that
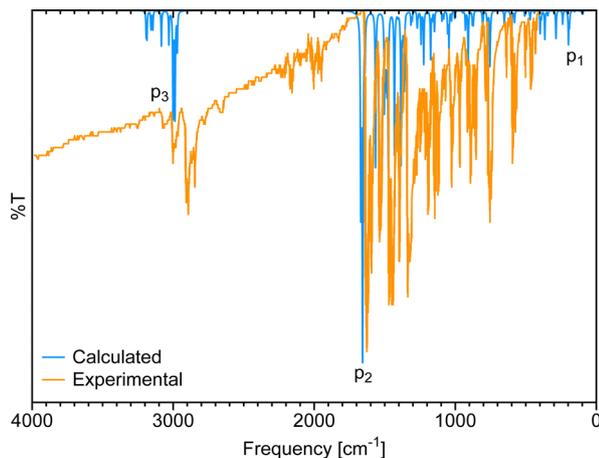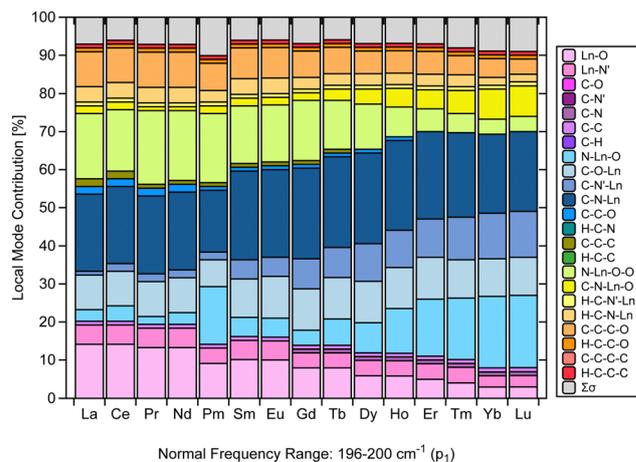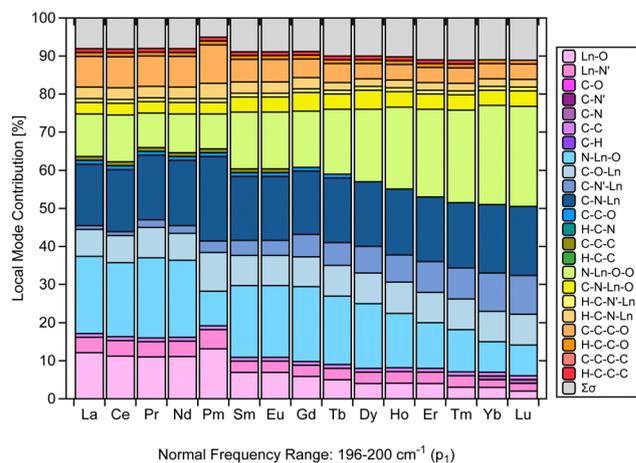

Fig. 3 Comparison of the calculated IR spectrum at the B3LYP/MWB52/6-311++G** level of theory with the experimental ATR-IR spectrum[36] of [Eu(trensal)].

(a)

(b)

Fig. 4 CNM analysis of the degenerate E-symmetry normal vibrational modes (a) and (b) associated with p_1 along the La–Lu series at the B3LYP/MWBn(Ln)/6-311++G** level of theory.

these normal modes, which distort the first coordination sphere in [Yb(trensal)], are of E-symmetry.[35] Most striking is the substantial difference in the patterns of these normal modes of E-symmetry, as shown in Fig. 4.

By comparing Fig. 4a and b, we can infer that the breaking of the C_3 symmetry occurs through motions with varying degrees of distortion in the first coordination sphere along the lanthanide series. Also, the local mode contributions associated with the molecular fragments N–Ln–O–O, N–Ln–O, C–O–Ln, C–N'–Ln, and C–N–Ln exhibit opposite trends. In Fig. 4a, the percentage values of N–Ln–O–O show an overall decrease, while those of N–Ln–O show an increase. However, this pattern is reversed in Fig. 4b. For C–O–Ln, C–N'–Ln, and C–N–Ln, the ascending trend observed in Fig. 4a shifts to a descending trend in Fig. 4b.

Importantly, the CNM analysis was successful in identifying and quantifying the contributions of the molecular fragments involved in the motion described by the normal vibrational modes that distort the first coordination sphere. Fig. 4 is a particularly remarkable outcome in this regard, raising the possibility that CNM can quantitatively aid in the guided design

1798 | *Phys. Chem. Chem. Phys.*, 2025, **27**, 1794–1803

This journal is © the Owner Societies 2025

suggested in the literature.[35] This finding is reassuring, as it opens up future research endeavors focused on different ligands and substituent effects.

Vibrations related to the complex formation (p_2)

Another relevant aspect of this investigation is the critical examination of the assignment of the strong IR characteristic band typical of Ln(trensal), which is an experimental evidence for the formation of the complex.[14,15,19–23] In this context, much of the assignments up to now has been qualitative in nature. The main challenge faced by qualitative assignments is the lack of a quantitative spectral analysis that assesses the composition of the characteristic normal vibrational modes.

Fig. 5 makes a considerable contribution to the characterization of [Ln(trensal)] by demonstrating, based on a strong theoretical framework, that the fingerprint normal vibrational modes indicative of [Ln(trensal)] formation in the frequency range of 1656–1658 cm^{-1} along the lanthanide series are composed not only of C–N contributions but also of C–C and H–C–N ones. In future investigations, we recommend using CNM to interpret vibrational spectra for the assignment of peaks that indicate the formation of Ln-containing complexes.

C–H vibrations (p_3)

Another finding that stands out from the results is the CNM analysis depicted in Fig. 6, which confirms that the C–H stretching vibrations in [Ln(trensal)] are nicely decoupled from other stretching, bending, or torsional vibrations.[31] The normal vibrational modes within 2984–2992 cm^{-1} along the La–Lu series are fully localized with respect to the C–H family. It is crucial to consider vibrational modes leading to non-radiative deactivation of excited states, as seen in [Eu(trensal)], where C–H high energy oscillators lead to undesired energy dissipation and luminescence quenching.[36] Because local vibrational modes are related to the local modes of overtone spectroscopy,[31,67] further studies are needed and highly recommended to test the monitoring of C–H
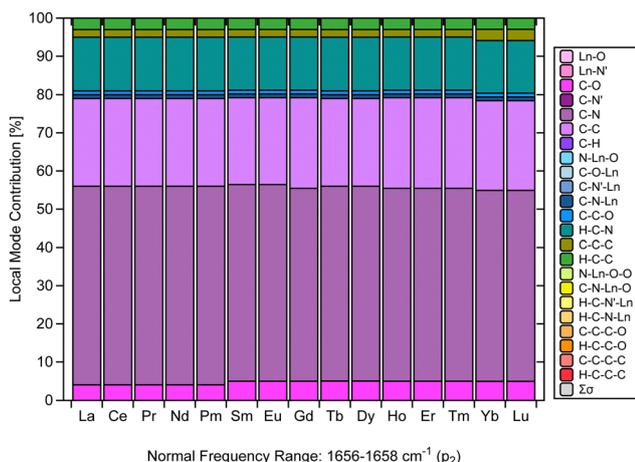

Fig. 5 CNM analysis of the normal vibrational mode associated with p_2 along the La–Lu series at the B3LYP/MWBn(Ln)/6-311++G** level of theory.
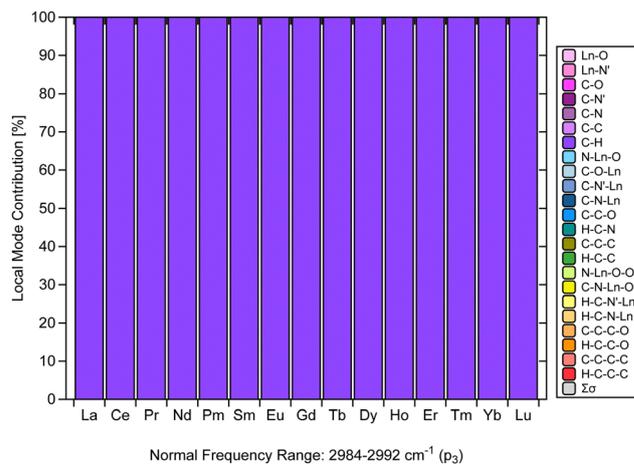

Fig. 6 CNM analysis of the normal vibrational mode associated with p_3 along the La–Lu series at the B3LYP/MWBn(Ln)/6-311++G** level of theory.

stretching vibrations in [Ln(trensal)] (and other complexes as well) *via* local mode analysis. This approach can conceivably be hypothesized to be relevant to strategies, such as deuteration or fluorination, for reducing undesired relaxation pathways aimed at the design of highly luminescent lanthanide complexes.[13]
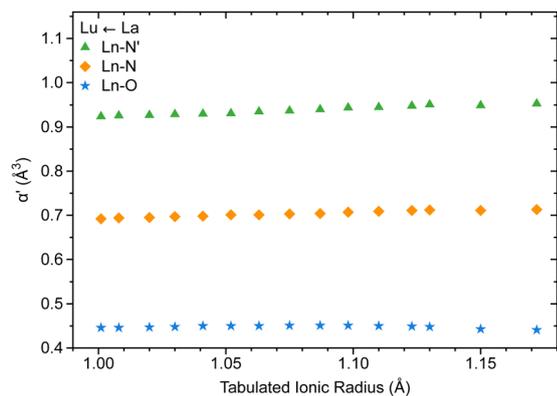
Relationships between bond properties

The C_3 point symmetry results in the equivalence between the oxygen atoms and the nitrogen atoms, except for the apical nitrogen within the coordination sphere of [Ln(trensal)], explaining the three families of lanthanide-ligand bonds depicted in Fig. 7.
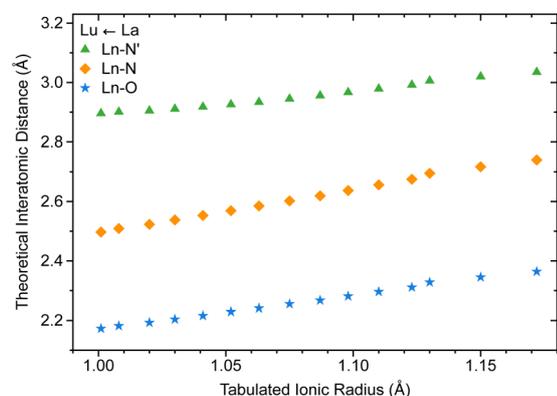
Recently, there has been renewed interest in Badger-type relationships, with implications for pairs of atoms in the periodic table, including lanthanides.[33] In this context, the knowledge from the literature that the coordination number of [Ln(trensal)] remains consistent throughout the lanthanide series is particularly relevant, as it enables relationships between ionic radii and interatomic distances within the coordination sphere.[15] It may be the case therefore that Fig. 7a supports this idea, as the ligand polarizabilities remain practically unchanged throughout the series, reflecting the consistency of polarization of the chemical environment around the Ln(III) ions.

Besides, Fig. 7b is in accord with a previous study indicating that interatomic distances within the coordination sphere decrease as the ionic radii decrease along the series.[15] However, caution must be applied, as interatomic distances alone cannot provide a reliable description of bond strength. This is where the local force constant plays a crucial role. The relationship between the local force constant and ionic radius in Fig. 7c suggests that the intrinsic strength of Ln–O and Ln–N bonds follows an inverse correlation with the ionic radius. Closer inspection of Fig. 7c raises the possibility that Ln–N′ bonds follow the opposite trend, prompting an investigation into the relationship between the local force constant and interatomic distance.
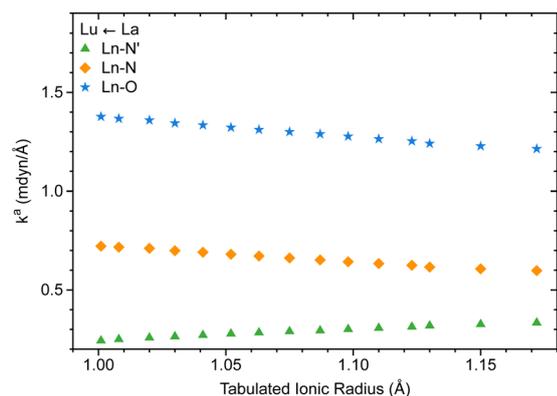
Fig. 8a and b indicate that Ln–O and Ln–N bonds adhere to the generalized Badger's rule along the lanthanide series;

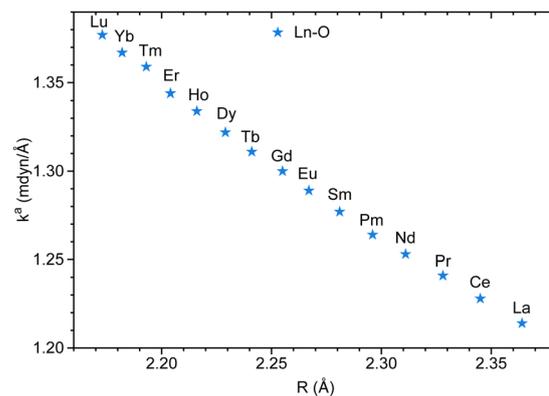This journal is © the Owner Societies 2025

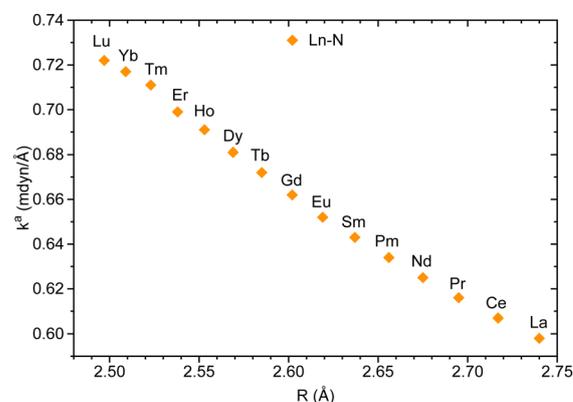*Phys. Chem. Chem. Phys.*, 2025, **27**, 1794–1803 | **1799**

Fig. 7 Ln(III)−L effective polarizability (a), interatomic distance (b), and local force constant (c) *vs.* Ln(III) ionic radius along the lanthanide series (Lu ← La). The results were obtained at the B3LYP/MWBn(Ln)/6-311++G** level of theory.

Fig. 8 Ln(III)−L local force constant *vs.* interatomic distance for Ln−O (a), Ln−N (b), and Ln−N′ (c) bonds. The results were obtained at the B3LYP/MWBn(Ln)/6-311++G** level of theory.

namely, the shorter the interatomic distance, the stronger the interaction. What stands out is Fig. 8c, where Ln−N′ follows the opposite trend. In accordance with the present results, previous studies have demonstrated that a shorter bond is not necessarily a stronger bond.[29,68–74] This intriguing finding may be attributed to the specific nature of the bond involving the apical nitrogen.
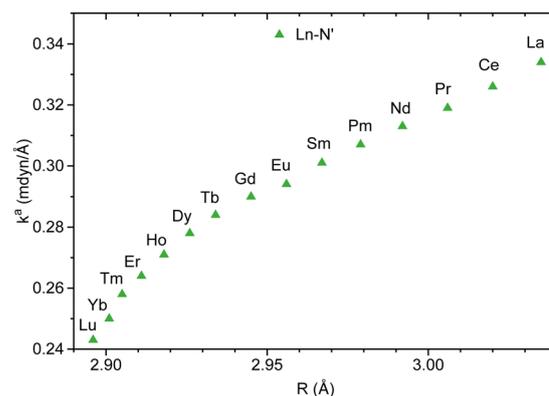
In Fig. S1 in the ESI,† experimental interatomic distances for the structural parameters within the coordination sphere of

[Ln(trensal)], taken from the literature,[18] are correlated with the corresponding B3LYP/MWBn(Ln)/6-311++G** values throughout the series. Because experimental data on [La(trensal)] and [Pm(trensal)] are not reported in the literature from which we took the structural parameters for comparison,[18] they are omitted from Fig. S1 (ESI†). There is a linear relationship between the experimental and theoretical quantities for the Ln−O, Ln−N, and Ln−N′ bonds (correlation coefficient, $r^2 >$ 0.9), which reassures that our calculated gas-phase structures are

1800 | *Phys. Chem. Chem. Phys.*, 2025, **27**, 1794–1803

This journal is © the Owner Societies 2025

Table 1 Comparison between the interatomic distance (R) and local force constant (k^a) of M–L bonds in [M(trensal)] complexes of trivalent Er and Fe ions

	[M(trensal)]				
	M = Er(III)[a]			M = Fe(III)[b]	
M–L	R (Å)	k^a (mdyn Å^{-1})		R (Å)	k^a (mdyn Å^{-1})
M1–O3	2.204	1.344		1.913	1.570
M1–O5	2.204	1.344		1.921	1.725
M1–O6	2.204	1.344		1.898	1.725
M1–N′2	2.911	0.264		3.607	0.265
M1–N4	2.538	0.699		2.034	1.321
M1–N7	2.538	0.699		2.036	1.179
M1–N19	2.538	0.699		2.006	1.422

[a] At the B3LYP/MWB57(Er)/6-311++G** level of theory. [b] At the UB3LYP/6-311++G** level of theory with a spin multiplicity of a doublet.

consistent with crystallographic structural characterization.[16–18] Fig. S2 (ESI†) offers insights into [Gd(trensal)], demonstrating that our calculations produced interatomic distances more closely related to the atomic radii.[64]

To date, research has tended to focus on the Ln–N′ interatomic distance rather than the intrinsic strength to assess the change in denticity for the complexation of trensal to the smaller trivalent transition-metal ions, leading to a distorted octahedron.[16,18] In light of local vibrational mode theory, the local force constant can contribute to a better understanding of the bonding involving the apical nitrogen. For the sake of computational convenience, [Fe(trensal)] has been selected to probe the hexadentate coordination expected for first-row transition metals. What can be clearly seen in Table 1 is the manifestation of the three-fold symmetry relating the equivalent nitrogen and oxygen atoms in [Er(trensal)], with a marked difference in both interatomic distance and local force constant for the Er–N′ bond.

The [Er(trensal)] complex was selected because it presents the local force constant value for the Er–N′ bond that closely matches that of the Fe–N′ bond in [Fe(trensal)]. What is striking in Table 1 is the dramatic difference in interatomic distance between Er–N′ and Fe–N′, despite their corresponding local force constant values being practically equivalent. Once again, this emphasizes that interatomic distance is not always a reliable descriptor of bond strength. These results therefore need to be interpreted with caution. Despite the similarity in intrinsic strength between Er–N′ and Fe–N′, the three equivalent Er–N bonds are more than twice as strong as Er–N′. For [Fe(trensal)], the weakest of the Fe–N bonds in the distorted octahedron is more than four times as strong as Fe–N′. This discrepancy in intrinsic strength could be attributed to the apical nitrogen not being bound in [Fe(trensal)], offering an alternative explanation for this change in denticity for the first time.

Conclusions

In this investigation, our primary objective was to utilize the characterization of normal mode (CNM) procedure from local vibrational mode theory to assess the normal vibrational modes that characterize the formation of the complex, the distortions in the first coordination sphere, and C–H vibrations of Ln(III) complexes, specifically [Ln(trensal)], along the lanthanide series. Our secondary aim was to combine the bond overlap model with local vibrational mode theory to analyze the chemical bonding within the coordination sphere of [Ln(trensal)]. The following key contributions should be emphasized:

● We have characterized the *E*-symmetry normal vibrational modes that distort the first coordination sphere in [Ln(trensal)], revealing the varying degrees of such distortions along the La–Lu series for the first time. This discovery is promising as it opens avenues for researches on different ligands and substituent effects, suggesting that CNM can quantitatively support guided design as proposed in the literature.[35]

● We have critically examined the assignment of the strong infrared band of [Ln(trensal)], which has been used experimentally as evidence for the formation of the complex.[14,15,19–23] We recommend using CNM to interpret vibrational spectra for assigning peaks indicative of Ln-containing complex formation in future studies.

● We have confirmed that the C–H stretching vibrations in [Ln(trensal)] are effectively decoupled from other stretching, bending, or torsional vibrations. This finding motivates further CNM studies aimed at minimizing undesired relaxation pathways.

● We have demonstrated that a shorter Ln–N′ bond does not indicate a stronger bond, which may be due to the unique features of the bond involving the apical nitrogen.

● For the first time, we have provided an alternative explanation based on the local force constant for the change in denticity of the trensal ligand when complexed to Fe(III).

Altogether, these findings enhance our understanding of the vibrational spectroscopy and chemical bonding of lanthanide complexes, offering valuable insights for future research.

Data availability

The data supporting this article have been included as part of the ESI.† Also, the codes utilized in this manuscript can be downloaded and accessed at **http://www.gpqtc.chembos.website/**.

Conflicts of interest

There are no conflicts to declare.

Acknowledgements

This journal is © the Owner Societies 2025

Phys. Chem. Chem. Phys., 2025, **27**, 1794–1803 | **1801**

References

1 R. A. Rocha, K. Alexandrov and C. Scott, *Microb. Biotechnol.*, 2024, **17**, e14503.

2 S.-L. Liu, H.-R. Fan, X. Liu, J. Meng, A. R. Butcher, L. Yann, K.-F. Yang and X.-C. Li, *Ore Geol. Rev.*, 2023, **157**, 105428.

3 D. Gielen and M. Lyons (2022), *Critical materials for the energy transition: Rare earth elements*, International Renewable Energy Agency, Abu Dhabi.

4 J.-C. G. Bünzli, *Coord. Chem. Rev.*, 2015, **293–294**, 19–47.

5 S. Cotton, *Lanthanide and Actinide Chemistry*, John Wiley & Sons, 2006.

6 T. Vitova, P. Roesky and S. Dehnen, *Commun. Chem.*, 2022, **5**, 12.

7 Z. Konkoli and D. Cremer, *Int. J. Quantum Chem.*, 1998, **67**, 1–9.

8 R. T. Moura Jr., M. Quintano, C. V. Santos-Jr, V. A. Albuquerque, E. C. Aguiar, E. Kraka and A. N. Carneiro Neto, *Opt. Mater.*, 2022, **16**, 100216-1-100216-15.

9 A. N. Carneiro Neto, R. T. Moura Jr., E. C. Aguiar, C. V. Santos and M. A. F. L. B. de Medeiros, *J. Lumin.*, 2018, **201**, 451–459.

10 R. T. Moura Jr., A. N. Carneiro Neto, R. L. Longo and O. L. Malta, *J. Lumin.*, 2016, **170**, 420–430.

11 N. Gündüz, T. Gündüz, M. Hursthouse, H. G. Parkes, L. S. Shaw (née Gözen), R. A. Shaw and M. Tüzün, *J. Chem. Soc. Perkin Trans. II*, 1985, 899–902.

12 D. M. Driscoll, F. D. White, S. Pramanik, J. D. Einkauf, B. Ravel, D. Bykov, S. Roy, R. T. Mayes, L. H. Delmau, S. K. Cary, T. Dyke, A. Miller, M. Silveira, S. M. VanCleve, S. M. Davern, S. Jansone-Popova, I. Popovs and A. S. Ivanov, *Nature*, 2024, **629**, 819–823.

13 E. Kreidt, C. Kruck and M. Seitz, *Handbook on the Physics and Chemistry of Rare Earths*, Elsevier, 2018, vol. 53, pp. 35–79.

14 M. Kanesato, T. Yokoyama, O. Itabashi, T. M. Suzuki and M. Shiro, *Bull. Chem. Soc. Jpn.*, 1996, **69**, 1297–1302.

15 M. Kanesato and T. Yokoyama, *Chem. Lett.*, 1999, 137–138.

16 P. V. Bernhardt, B. M. Flanagan and M. J. Riley, *Aust. J. Chem.*, 2000, **53**, 229–231.

17 B. M. Flanagan, P. V. Bernhardt, E. R. Krausz, S. R. Lüthi and M. J. Riley, *Inorg. Chem.*, 2001, **40**, 5401–5407.

18 B. M. Flanagan, P. V. Bernhardt, E. R. Krausz, S. R. Lüthi and M. J. Riley, *Inorg. Chem.*, 2002, **20**, 5024–5033.

19 S. Salehzadeh, S. M. Nouri, H. Keypour and M. Bagherzadeh, *Polyhedron*, 2005, **24**, 1478–1486.

20 C. D. Buch, D. Mitcov and S. Piligkos, *Dalton Trans.*, 2020, **49**, 13557–13565.

21 C. D. Buch, S. H. Hansen, C. M. Tram, D. Mitcov and S. Piligkos, *Inorg. Chem.*, 2020, **59**, 16328–16340.

22 C. D. Buch, S. H. Hansen, D. Mitcov, C. M. Tram, G. S. Nichol, E. K. Brechin and S. Piligkos, *Chem. Sci.*, 2021, **12**, 6983–6991.

23 Y. Zhou, C. D. Buch, S. H. Hansen and S. Piligkos, *Dalton Trans.*, 2023, **52**, 8792–8799.

24 M. Quintano and E. Kraka, *Chem. Phys. Lett.*, 2022, **803**, 139746-1-139746-7.

25 E. Kraka, M. Quintano, H. W. L. Force, J. J. Antonio and M. Freindorf, *J. Phys. Chem. A*, 2022, **126**, 8781–8900.

26 R. T. Moura, Jr., M. Quintano, J. J. Antonio, M. Freindorf and E. Kraka, *J. Phys. Chem. A*, 2022, **126**, 9313–9331.

27 M. Quintano, A. A. A. Delgado, R. T. Moura Jr, M. Freindorf and E. Kraka, *Electron Struct.*, 2022, **4**, 044005–1- 044005-17.

28 M. Quintano, R. T. Moura Jr. and E. Kraka, *Chem. Phys. Lett.*, 2023, **826**, 140654-1-140654-7.

29 M. Quintano, R. T. Moura Jr. and E. Kraka, *J. Mol. Model.*, 2024, **30**, 102.

30 M. Quintano, R. T. Moura Jr. and E. Kraka, *Chem. Phys. Lett.*, 2024, **849**, 141416.

31 E. Kraka, J. A. Larsson and D. Cremer, *Computational Spectroscopy*, Wiley, New York, 2010, pp. 105–149.

32 A. Madushanka, R. T. Moura, Jr., N. Verma and E. Kraka, *Int. J. Mol. Sci.*, 2023, **24**, 6311.

33 D. L. Crittenden, *AIP Adv.*, 2023, **13**, 115323.

34 R. G. Parr and Y. Weitao, *Density-Functional Theory of Atoms and Molecules*, Oxford University Press, 1994.

35 J. G. C. Kragskow, J. Marbey, C. D. Buch, J. Nehrkorn, M. Ozerov, S. Piligkos, S. Hill and N. F. Chilton, *Nat. Commun.*, 2022, **13**, 825.

36 S. K. Kuppusamy, E. Vasilenko, W. Li, J. Hessenauer, C. Ioannou, O. Fuhr, D. Hunger and M. Ruben, *J. Phys. Chem. C*, 2023, **127**, 10670–10679.

37 Z. Konkoli and D. Cremer, *Int. J. Quantum Chem.*, 1998, **67**, 29–40.

38 E. Kraka, W. Zou and Y. Tao, *WIREs: Comput. Mol. Sci.*, 2020, **10**, 1480.

39 E. B. Wilson, J. C. Decius and P. C. Cross, *Molecular Vibrations: The Theory of Infrared and Raman Vibrational Spectra*, McGraw-Hill, New York, 1955.

40 E. B. Wilson, *J. Chem. Phys.*, 1941, **9**, 76–84.

41 W. Zou and D. Cremer, *Chem. Eur. J.*, 2016, **22**, 4087–4097.

42 W. Zou, R. Kalescky, E. Kraka and D. Cremer, *J. Chem. Phys.*, 2012, **137**, 084114.

43 C. K. Jørgensen and B. R. Judd, *Mol. Phys.*, 1964, **8**, 281–290.

44 S. F. Mason, R. D. Peacock and B. Stewart, *Mol. Phys.*, 1975, **30**, 1829–1841.

45 B. R. Judd, *J. Chem. Phys.*, 1979, **70**, 4830–4833.

46 C. Santos-Jr and R. Moura Jr., *ChemRxiv*, 2023, 1–21.

47 R. T. Moura Jr., A. N. C. Neto, O. L. Malta and R. L. Longo, *J. Mol. Model.*, 2020, **26**, 301.

48 C. V. Santos-Jr, E. M. Lima and R. T. Moura Jr., *Comput. Theor. Chem.*, 2021, **1206**, 113457.

49 C. V. Santos-Jr, M. A. F. de Souza, E. Kraka and R. T. Moura Jr., *Chem. Phys. Lett.*, 2022, **787**, 139282.

50 C. V. Santos, S. A. Monteiro, A. S. C. Soares, I. C. A. Souto and R. T. Moura Jr., *J. Phys. Chem. A*, 2023, **127**, 7997–8014.

51 C. V. Santos-Jr, G. M. B. Da Silva, R. P. Dias, R. T. Moura Jr. and J. C. S. Da Silva, *Adv. Theory Simul.*, 2024, **7**(5), 2301148.

52 W. G. Barbosa, C. V. Santos-Jr, R. B. Andrade, J. R. Lucena Jr and R. T. Moura Jr, *J. Mol. Model.*, 2024, **30**, 139.

53 W. Thor, A. N. Carneiro Neto, R. T. Moura Jr., K.-L. Wong and P. A. Tanner, *Coord. Chem. Rev.*, 2024, **517**, 215927.

54 A. D. Becke, *J. Chem. Phys.*, 1993, **98**, 5648–5652.

55 C. Lee, W. Yang and R. G. Parr, *Phys. Rev. B: Condens. Matter Mater. Phys.*, 1988, **37**, 785–789.

56 R. Krishnan, J. S. Binkley, R. Seeger and J. A. Pople, *J. Chem. Phys.*, 1980, **72**, 650–654.

57 T. Clark, J. Chandrasekhar, G. W. Spitznagel and P. V. R. Schleyer, *J. Comput. Chem.*, 1983, **4**, 294–301.

58 M. Dolg, H. Stoll and H. Preuss, *J. Chem. Phys.*, 1989, **90**, 1730–1734.

59 M. J. Frisch, G. W. Trucks, H. B. Schlegel, G. E. Scuseria, M. A. Robb, J. R. Cheeseman, G. Scalmani, V. Barone, G. A. Petersson and H. Nakatsuji *et al.*, *Gaussian 16 Revision C.01*, 2016, Gaussian Inc., Wallingford CT.

60 T. Lu and F. Chen, *J. Comput. Chem.*, 2012, **33**, 580–592.

61 C. V. Santos-Jr, E. M. Lima and R. T. Moura Jr., *Comput. Theor. Chem.*, 2021, **1206**, 113457.

62 W. Zou, R. Moura Jr., M. Quintano, F. Bodo, Y. Tao, M. Freindorf, M. Z. Makoś, N. Verma, D. Cremer and E. Kraka, *LModeA2023, Computational and Theoretical Chemistry Group (CATCO)*, Southern Methodist University, Dallas, TX, USA, 2023.

63 E. C. Meng, T. D. Goddard, E. F. Pettersen, G. S. Couch, Z. J. Pearson, J. H. Morris and T. E. Ferrin, *Protein Sci.*, 2023, **32**, e4792.

64 R. D. Shannon, *Acta Crystallogr., A*, 1976, **32**, 751–767.

65 C. Adamo and V. Barone, *J. Chem. Phys.*, 1999, **110**, 6158–6170.

66 V. Vetere, C. Adamo and P. Maldivi, *Chem. Phys. Lett.*, 2000, **325**, 99–105.

67 D. Cremer and E. Kraka, *Curr. Org. Chem.*, 2010, **14**, 1524–1560.

68 E. Kraka, D. Setiawan and D. Cremer, *J. Comput. Chem.*, 2015, **37**, 130–142.

69 D. Setiawan, E. Kraka and D. Cremer, *J. Phys. Chem. A*, 2015, **119**, 9541–9556.

70 E. Kraka and D. Cremer, *Rev. Proc. Quim.*, 2012, 39–42.

71 D. Cremer, A. Wu, J. A. Larsson and E. Kraka, *J. Mol. Model.*, 2000, **6**, 396–412.

72 M. Kaupp, B. Metz and H. Stoll, *Angew. Chem., Int. Ed.*, 2000, **39**, 4607–4609.

73 M. Kaupp and S. Riedel, *Inorg. Chim. Acta*, 2014, **357**, 1865–1872.

74 B. A. Lindquist and T. H. Dunning, Jr., *J. Phys. Chem. Lett.*, 2013, **4**, 3139–3143.

This journal is © the Owner Societies 2025

Phys. Chem. Chem. Phys., 2025, **27**, 1794–1803 | **1803**